A mathematical framework for the detection of localized anomalies in the Young's modulus of a rod

Bryl Nico M. Ong[1], Aarush Borker[2], Neil Jerome A. Egarguin*[1], and Daniel Onofrei[3]

[1]Institute of Mathematical Sciences, University of the Philippines Los Banos, Laguna, 4031 Philippines
[2]Mahwah High School, Mahwah, NJ, 07430 USA
[3]Department of Mathematics, University of Houston, Houston, TX, 77004 USA

ABSTRACT

A critical issue that affects engineers trying to assess the structural integrity of various infrastructure, such as metal rods or acoustic ducts, is the challenge of detecting internal fractures (defects). Engineers typically rely on audible and visual inspection to detect these anomalies, as destructive testing is impractical. This study proposes a robust and non-invasive strategy to characterize such defects using only a small set of minimal measurements.

Assuming a one-dimensional model, we make use of the continuous one-dimensional wave equation to model these physical phenomena and then employ specialized mathematical analysis tools (the Laplace transform and optimization) to introduce our defect characterization ideas. In particular, we will focus on the case of a long rod which is homogeneous throughout except in a small area where a defect in its Young's modulus is present. We will first demonstrate how the problem is equivalent to a spring-mass vibrational system. Afterwards, we show how our imaging strategy makes use of the Laplace domain analytic map between the characteristics of the respective defect and the measurement data.

More explicitly, we will utilize MATLAB to generate synthetic data as a computational surrogate for actual physical measurements in several scenarios with one defect of arbitrary location and stiffness. Subsequently, we will use this data along with our analytically developed map (between defect characteristics and measurements) to construct a residual function which, once optimized, will reveal the location and magnitude of the stiffness defect.

INTRODUCTION

Maintaining the integrity of infrastructure, such as bridges, drainage, and aerospace components, relies on the ability to identify hidden defects using non-destructive methods. Current non-destructive evaluation (NDE) techniques employ various forms of vibrational analysis due to their cost-effectiveness and reliability (see for instance Cawley and Adams 1979, Shifrin 2017, Zhang et al 2018, Peng et al 2022, Zou et al 2000). Specifically, many methods employ one-dimensional spring-mass analogues and wave equation models. These solutions are notable for their intuitive physical representation, analytical versatility (resulting from the Laplace transform), and especially their straightforward implementation in various numerical software, such as MATLAB. In biomechanics and computer graphics, spring-mass networks can simulate soft-tissue deformation and cloth dynamics in real-time, sacrificing system continuity for computational speed and robustness (Dimarogonas 1996). Moreover, acoustic metamaterials use one-dimensional (1D) spring-mass chains to block specific sound frequencies, thus creating an acoustically manipulable system (Palacz and Krawczuk 2002). Even vehicle and vibrational suspension systems employ a discrete set of springs and masses to identify and isolate harmful fluctuations arising from dynamic loads (Dilena and Morassi 2009).

An emerging area of NDE research focuses on treating internal cracks, or defects, as an extra spring. When measuring certain values of such systems, the spring associated with the crack perturbs natural frequencies, thus shifting the poles of a system's Laplace- domain output (Rubio et al 2015). Certain studies have already demonstrated that employing just two low-frequency measurements can be used to detect a single defect through a singular formula (Cawley and Adams 1979). Recently, works use

*Corresponding author
Email Address: **naegarguin1@up.edu.ph**
Date received: 29 September 2025
Date revised: 11 December 2025
Date accepted: 24 December 2025
DOI: https://doi.org/10.54645/2026191URW-27

KEYWORDS

Spring-mass system, defect detection, Laplace transform, optimization

guided-wave Bayesian methods (Zeng et al 2023) and particle-swarm optimizers (Grebla et al 2023) to detect multiple and/or nonlinear defects.

On the other hand, many methods rely on continuous and precise Laplace-domain data, depend on closed-form inversion (valid for one or two defects), or struggle to generate an inverse map with boundary measurements and defect parameters. In reality, sensors may only monitor discrete time-series data, which is plagued by noise, and cracks can occur at arbitrary depths with varying magnitudes. As a result, the challenge of creating a data- driven imaging strategy that reliably recovers the location and size of a single defect from minimal, easily measurable data, while considering noise, remains unsolved.

Despite these advances, one can note that existing approaches face practical limitations, especially when they are applied to cases involving noisy boundary measurements.

In this work, we study the inverse problem of locating and quantifying a localized stiffness defect in a one–dimensional elastic rod using only a single endpoint displacement trace. The forward model is the standard 1D longitudinal wave equation discretized by a lumped spring–mass chain (e.g., in our particular numerical setup, length $L = 1$ meter, $N = 100$ nodes, $\Delta x = \frac{L}{N}$). The inverse task is to recover the index j and the local spring constant k^* of a single anomalous element from noisy measurements of the left-end displacement $u_0(t)$ produced by an impulsive initial velocity.

Our numerical results show the inversion recovers the defect location exactly (to the discretization cell) and recovers k^* with relative errors $\lesssim 0.1\%$ under realistic Gaussian measurement noise up to $\sigma = 10^{-5}$ m. The discrete contrast k^* maps directly to a continuum Young's modulus in the defective element via $E_{\text{def}} = \frac{k^*\Delta x}{A}$; consequently results for $k^* \in [0.1, 5]$ correspond to $\frac{E_{\text{def}}}{E_0} \in [0.1, 5]$ in the continuum model.

The key features of our approach are:

- a hybrid Laplace-domain forward solver that yields cheap, high-fidelity forward responses used to build a synthetic measurement map,
- a robust inversion pipeline that combines a coarse per-index search with a local non-linear refine (Gauss–Newton / constrained optimization) and simple smoothing regularization of the forward data; and
- an extensive validation campaign (Monte Carlo noise sweeps, contrast sweeps, and sensitivity to parameter mismatch) that quantifies the practical detection limits.

This work builds on our previous works (Egarguin et al 2020, Egarguin et al 2022) and attempts to make a step towards addressing these issues in the context of the problem of determining the location and size of a defect in the Young's modulus of a long rod which is otherwise homogeneous. The said previous works dealt with defects in an acoustic duct which translates to defects in the mass of some bodies in a spring-mass system. Meanwhile, this work focuses on analyzing the defects in the Young's modulus in a rod, which is approximated by defective springs in a 1D spring-mass system. We will start by showing the quantitative equivalence between a metal homogeneous rod with a localized defect in its Young's modulus and a 1D homogeneous spring-mass system with a defective spring constant. Thus, an impulsive force at the left end of the rod will result in a longitudinal wave propagating along the rod and subsequent vibrations being measured at the left end point. Equivalently, the discrete system activated by an initial impulse applied at its first mass will generate vibrations through the entire system. Then, in this discrete setup, measurements will consist of the resulting vibrations of the first mass. As shown in (Egarguin et al 2022), through a z −transform approach one can use the set of discrete time measurements of the first mass and obtain an approximation of the Laplace transform of the first mass vibrations (when perceived as a function of time).

We then proceed towards building the analytic map relating the defective spring constant (defect size) and its location to the vibrations of the first mass. Then, in the Laplace domain, a residual functional is proposed measuring the discrepancy between this analytic map the synthetic measurements data set (i.e., the Laplace transform of the first mass vibrations). Finally, minimization of this residual functional determines both the location and magnitude of the stiffness defect. All of this is achieved with minimal, non-invasive data, as measurements are only taken from one end of the system. In the context of a metal rod, our results show how vibrational data resulting from an impulsive force at one end of the rod will indicate the position and level of abnormal Young's modulus at one point in the rod which in turn offers a prediction for the position and likelihood of a future crack occurring at that point.

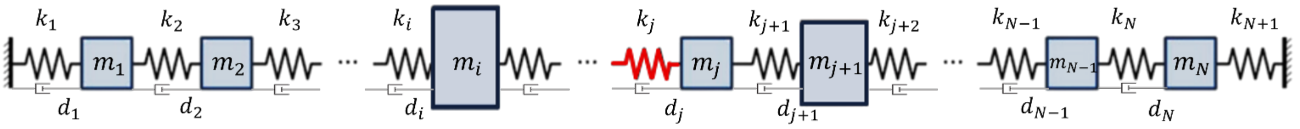

Figure 1: Discrete spring–mass chain model of a 1D bar with a single stiffness defect (high- lighted spring). Each mass represents a segment of the bar and each spring its local stiffness $\boldsymbol{k_i}$.

Our proposed method shares similarities with previous works that evaluate vibrational NDE by modeling defects as local compliance using a 1D spring-mass system combined with Laplace-domain analysis (Cawley and Adams 1979, Rubio et al 2015). Similar to Zeng et al. (2023), our method inverts boundary wave measurements. The method determines defect parameters: the defect's position along the system and its severity. Severity is indicated by the deviation of the spring constant from that of the homogeneous system. Unlike a Bayesian posterior that updates with each new observation, our residual minimization function can be optimized to identify both the size and location of the defect using only minimal, discrete endpoint measurements. An analytic inverse-spectral method was employed in (Shifrin 2017) and closed-form techniques were used in (Rubio et al 2015) to identify one or two defects from frequency data. In (Egarguin et al 2022) the authors used the poles of the transfer function to detect one or two defects with left hand measurements in a system activated by an impulsive force. The method we propose can handle arbitrary defect positions in a single-defect scenario with discrete data and our numerics suggest it is extensible to the case of arbitrary number of defects. Additionally, unlike forward-only spectral-element methods (see Palacz and Krawczuk 2002, Krawczuk et al 2006, Zhang et al 2018, Liu et al 2023) and frequency-shift reconstructions (Dilena and Morassi 2009), our approach develops an explicit inverse mapping from endpoint vibrational data to infer the defective spring constant and its position. In (Egarguin et al 2020) the authors built a similar analytic map relating the defect characteristics to the measurement data and identify one defect (size and location) or two defects if a priori information about their location or sizes is offered. In (Egarguin et al 2022) the authors use the defect signature on the poles of the transfer function, although the method proposed there requires continuous spectral data. Both of these approaches extend the concept of using a spring-mass system within a Laplace- domain framework. Notably, while newer methods employ guided-wave Bayesian inference or particle-swarm analysis for defect identification (Zeng et al 2023, Grebla et al 2023), our method is computationally cheap and maintains accuracy even with noisy and discrete data.

METHODS

This section presents the mathematical framework used to identify the size and location of defects in otherwise homogeneous hyperbolic linear systems. More explicitly, we consider two one-dimensional wave propagation models. The first one models transverse waves (string with fixed ends) while the second deals with longitudinal waves (long bar with clamped ends). Each model contains one defect of unknown size and location (defective localized string tension and respectively defective localized Young's modulus). First, we show how each of these two models can be equivalently represented by a discrete spring–mass system where one spring has a defective spring constant. Then we will develop a new strategy to detect the position and size of the defective spring constant resulting, through the above equivalence, in a strategy to detect the defective location and size in the string tension or the elastic bar's Young's modulus, respectively.

We will proceed first to describe the main paradigm in the context of a discrete spring and mass system.

Discrete Spring–Mass–Damper Chain

We model our structure as a chain of N point masses $m_1, \dots, m_N$ connected in series by linear springs and dashpots. Mass m_j sits between springs of stiffness k_j (to the left) and k_{j+1} (to the right), and dashpots of damping d_j and d_{j+1} (see Figure 1). Denote its displacement by $x_j(t)$. Newton's second law at each interior mass $j = 1, \dots, N$ gives (see Egarguin et al 2020, Egarguin et al 2022)

$$\begin{cases} m_1 x_1''(t) = -k_1 x_1 - d_1 x_1' + k_2(x_2 - x_1) + \gamma\delta(t) \\ m_j x_j''(t) = k_j\left(x_{j-1} - x_j\right) - d_j x_j' + k_{j+1}\left(x_{j+1} - x_j\right) \text{ for } j = 2, 3, \dots, N-1 \\ m_N x_N''(t) = -k_{N+1} x_{\square\square} - d_N x_N' - k_N(x_N - x_{N-1}) \end{cases}$$

where $\delta(t)$ denotes the Dirac distribution centered at zero. Recall that $\delta(t)$ can be heuristically described as the generalized function with $\delta(t) = 0$ for all $t \neq 0$ and $\int_{-\infty}^{+\infty} \delta(t)\, dt = 1$. In the previous system of equations, we also assumed that the system is driven by an impulsive force acting on the first mass with prescribed amplitude γ.

Rearranging, this can be written in the compact tridiagonal form:

$$x_j'' = \frac{k_j}{m_j} x_{j-1} - \frac{k_j + k_{j+1}}{m_j} x_j + \frac{k_{j+1}}{m_j} x_{j+1} - \frac{d_j}{m_j} x_j' + f_j, \qquad \text{for } j = 1, 2, \dots, N, \tag{1}$$

where $f_1(t) = \gamma\delta(t)$, $f_2 = \dots = f_N = 0$ represents the impulsive forcing term. In Equation (1) we assumed the convention that $(x_0(t) = x_{N+1}(t) = 0)$.

This discrete spring–mass–damper model serves as our reference. In Section 2.2 and Section 2.3, we will demonstrate that applying centered finite differences to the continuous 1D wave PDEs (string and bar) yields exactly these same equations once we set

$$m_i = \rho(x_i)\Delta x, \qquad k_i = \frac{\text{local stiffness at } x_i}{\Delta x}, \quad d_j = \frac{\text{local damping at } x_i}{\Delta x}, \quad \text{for } i = 1, 2, \dots, N.$$

In the next two sections, we shall discuss the analogy of transverse strings (Section 2.2) and heterogenous bars (Section 2.3) to spring-mass-damper systems (SMDS). Although the discussions in Section 2.2 and Section 2.3 are very similar since the underlying equations governing the respective vibration profiles are exactly the same, we chose to present each topic separately to highlight the physical difference between the two types of situations we address. In Section 2.2, we shall show that the tension in a point in the string can be discretely modelled as a stiffness constant of a spring in an SMDS. Meanwhile, we show in Section 2.3 how the proportionality constant between stress and strain in linear elastic media (i.e., the Young's modulus) translates to a spring stiffness in an SMDS.

Transverse String and its Spring–Mass–Damper Analogue

We begin with the most general 1D transverse- wave equation modelling the time- varying vibration profile u in a clamped string modeled as a one-dimensional segment $[0, L]$, and whose linear density $\rho_0(x)$, tension $T(x)$, and damping $\mu(x)$ vary with position:

$$\frac{\partial^2 u}{\partial t^2} = \frac{1}{\rho_0(x)} \frac{\partial}{\partial x}\left(T(x)\frac{\partial u}{\partial x}\right) - \frac{\mu(x)}{\rho_0(x)} \frac{\partial u}{\partial t} \tag{2}$$

with boundary data given by $u(0,t) = u(L,t) = 0$ and activated by impulsive initial data, i.e. $u(x,0) = 0, u'(x,0) = \gamma\delta(x)$. Sampling at equally spaced points $x_i = i\Delta x$, for $i = 0, 1, \dots, N+1$, (i.e., $(N+1)\Delta x = L$), letting $\rho_i = \rho_0(x_i)$, $T_i = T(x_i)$, $\mu_i = \mu(x_i)$, and $u_i \approx u(x_i, t)$, and applying a forward finite difference approximation for $\frac{\partial u}{\partial x}$ we obtain the following finite difference approximation for the spatial derivative $\frac{\partial}{\partial x}\left(T(x)\frac{\partial u}{\partial x}\right)$:

$$\left.\frac{\partial}{\partial x}(T u_x)\right|_{x=x_i} \approx \frac{T_{i+1}u_{i+1} - (T_i + T_{i+1})u_i + T_i u_{i-1}}{(\Delta x)^2}, \quad i = 1, 2, \dots, N.$$

If we let $u_i'' = \frac{d^2 u_i}{dt^2}$ and $u_i' = \frac{du_i}{dt}$, the discrete update reads

$$u_i'' = \frac{1}{\rho_i} \frac{T_{i+1}u_{i+1} - (T_i + T_{i+1})u_i + T_i u_{i-1}}{(\Delta x)^2} - \frac{\mu_i}{\rho_i} u_i', \quad i = 1, 2, \dots, N. \tag{3}$$

with the observation that the fixed end boundary conditions imply $u_0 = u_{n+1} = 0$.

On the other hand, from Equation (1) we have that the equation of motion for the i$^{\text{th}}$ mass $x_i(t)$ in a discrete chain of N masses $m_1, \ldots, m_N$ linked by springs $k_1, \ldots, k_{N+1}$ and dashpots $d_1, \ldots, d_N$, assuming that $x_0(t) = x_{N+1}(t) = 0$, is

$$x_i'' = \frac{k_i}{m_i} x_{i-1} - \frac{k_i + k_{i+1}}{m_i} x_i + \frac{k_{i+1}}{m_i} x_{i+1} - \frac{d_i}{m_i} x_i' + f_j, \quad i = 1, 2, \ldots, N. \tag{4}$$

Equations (3) and (4) coincide exactly under the identifications

$$m_i = \rho_i \Delta x, \;\; k_i = \frac{T_i}{\Delta x}, \;\; d_i = \mu_i \Delta x.$$

Therefore, each string segment of length Δx and density ρ_i becomes a discrete mass m_i, each local tension T_i becomes a spring stiffness constant k_i, and the continuous damping μ_i becomes the damping coefficient d_i. This one-to-one mapping showcases our defect-imaging strategy, which treats local changes in $T(x)$ as defective springs in the spring and mass chain. In particular, a localized modification in the string tension T_{j^*} corresponds to a defective spring k_{j^*} in the chain, enabling us to detect defect location and severity via spring–mass inversion.

Longitudinal Vibration in a Heterogeneous Bar and Its Spring–Mass Analogue

Consider axial vibrations $w(x,t)$ in a rod of length L whose density $\rho(x)$, Young's modulus $E(x)$, and damping $\mu(x)$ vary with position, that satisfies

$$\rho(x) \frac{\partial^2 w}{\partial t^2} = \frac{\partial}{\partial x}\left(E(x) \frac{\partial w}{\partial x}\right) - \mu(x) \frac{\partial w}{\partial t}, \tag{5}$$

where we assumed homogeneous Dirichlet boundary conditions $w(0,t) = w(L,t) = 0$ and the vibrations generated by an impulsive initial data, i.e., $w(x,0) = 0$; $w'(x,0) = \gamma\delta(x)$. We recall that as classically defined, the Young's modulus $E(x)$ is the proportionality constant between stress and strain in linear elastic media (with stress defined as the internal force per unit area and strain as the measure of elongation (gradient of the displacement)). We mention that the Young's modulus usually encodes the level of stress accumulation in the media.

We discretize Equation (5) with $x_i = i\Delta x$, $i = 0, \ldots, N+1$, $\Delta x = \frac{L}{N+1}$, and by setting $\rho_i = \rho(x_i)$, $E_i = E(x_i)$, $\mu_i = \mu(x_i)$, and writing $w_i(t) \approx w(x_i, t)$. A centered- difference approximation in x gives

$$\frac{\partial}{\partial x}(E w_x)\Big|_{x=x_i} \approx \frac{E_{i+1} w_{i+1} - (E_i + E_{i+1}) w_i + E_i w_{i-1}}{(\Delta x)^2}.$$

Hence, denoting $w_i'' = \frac{d^2 w_i}{dt^2}$, $w_i' = \frac{dw_i}{dt}$, the finite-difference update is

$$w_i'' = \frac{1}{\rho_i} \frac{E_{i+1} w_{i+1} - (E_i + E_{i+1}) w_i + E_i w_{i-1}}{(\Delta x)^2} - \frac{\mu_i}{\rho_i} w_i', \quad i = 1, \ldots, N, \tag{6}$$

with the observation that the fixed end boundary conditions imply $E_0 = E_{n+1} = 0$.

On the other hand, from equation (1) we have that the equation of motion for the i$^{\text{th}}$ mass $x_i(t)$ in a discrete chain of N masses $m_1, \ldots, m_N$ linked by springs $k_1, \ldots, k_{N+1}$ and dashpots $d_1, \ldots, d_N$, assuming that $x_0(t) = x_{N+1}(t) = 0$, is given by Equation (4). Equations (4) and (6) coincide exactly under the identifications

$$m_i = \rho_i \Delta x, \;\; k_i = \frac{E_i}{\Delta x}, \;\; d_i = \mu_i \Delta x.$$

Therefore, each string segment of length Δx and density ρ_i becomes a discrete mass m_i, each local Young's modulus E_i becomes a spring stiffness constant k_i, and the continuous damping μ_i becomes the damping coefficient d_i. This one-to-one mapping showcases our defect-imaging strategy, which treats local changes in $E(x)$ as defective springs in the spring and mass chain. In particular, a localized drop (or rise) in the bar's Young's modulus E_{j^*} corresponds to a defective spring k_{j^*} in the chain (highlighted in Figure 2), enabling us to detect defect location and severity via spring–mass inversion.

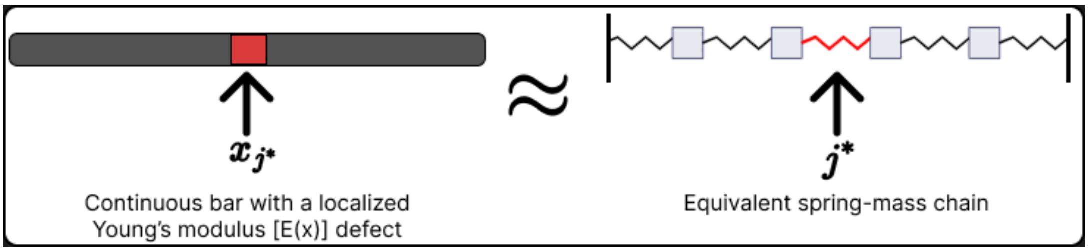

Figure 2: Left: a continuous bar with a localized Young's-modulus defect at x_{j^*}. **Right**: the equivalent spring–mass chain where the j^{th} spring has altered stiffness $k_{j^*} = \frac{E_{j^*}}{\Delta x}$.

Mathematical Framework for Characterizing Defective Springs in a Spring-mass System

We consider the system in equation (1) first under the homogeneous assumption and then a system with one defective spring constant. Thus, for the homogeneous system, i.e., when $m_j = 1, d_j = d, k_j = k$, driven by the impulsive force at the first mass, we have the following mathematical model (Egarguin et al 2020, Egarguin et al 2022):

$$\begin{cases} x_1'' + dx_1' + 2kx_1 - kx_2 & = \gamma\delta(t) \\ x_2'' + dx_2' + 2kx_2 - kx_1 - kx_3 & = 0 \\ \vdots & \\ x_j'' + dx_j' + 2kx_j - kx_{j-1} - kx_{j+1} & = 0 \\ \vdots & \\ x_{N-1}'' + dx_{N-1}' + 2kx_{N-1} - kx_{N-2} - kx_N & = 0 \\ x_N'' + dx_N' + 2kx_N - kx_{N-1} & = 0 \end{cases} . \qquad (7)$$

Now, suppose that all constants are equal to 1, except that of the spring at position j with a spring constant $k^* \neq 1$. Then the system becomes

$$\begin{cases} x_1'' + dx_1' + 2x_1 - x_2 & = \gamma\delta(t) \\ x_2'' + dx_2' + 2x_2 - x_1 - x_3 & = 0 \\ \vdots & \\ x_{j-1}'' + dx_{j-1}' + (1+k^*)x_{j-1} - x_{j-2} - k^*x_j & = 0 \\ x_j'' + dx_j' + (1+k^*)x_j - k^*x_{j-1} - x_{j+1} & = 0 \\ \vdots & \\ x_{N-1}'' + dx_{N-1}' + 2x_{N-1} - x_{N-2} - x_N & = 0 \\ x_N'' + dx_N' + 2x_N - x_{N-1} & = 0 \end{cases} . \qquad (8)$$

Taking the Laplace transform of the expressions in Equation (8) plus some algebraic manipulation yields

$$\begin{cases} (s^2 + ds + 2)\,\tilde{x}_1 - \tilde{x}_2 & = \gamma \\ (s^2 + ds + 2)\tilde{x}_2 - \tilde{x}_1 - \tilde{x}_3 & = 0 \\ \vdots & \\ \left(s^2 + ds + (1+k^*)\right)\tilde{x}_{j-1} - \tilde{x}_{j-2} - k^*\tilde{x}_j & = 0 \\ \left(s^2 + ds + (1+k^*)\right)\tilde{x}_j - k^*\tilde{x}_{j-1} - \tilde{x}_{j+1} & = 0 \\ \vdots & \\ (s^2 + ds + 2)\tilde{x}_{N-1} - \tilde{x}_{N-2} - \tilde{x}_N & = 0 \\ (s^2 + ds + 2)\tilde{x}_N - \tilde{x}_{N-1} & = 0 \end{cases} . \qquad (9)$$

Letting $h = -(s^2 + ds + 2)$ and performing some more algebraic manipulations allow us to write the System (9) into the matrix form

$$AX = b \qquad (10)$$

where A is the tridiagonal matrix given by

$$A = \begin{pmatrix} h & 1 & & & & & & & & \\ 1 & h & 1 & & & & & & & \\ 0 & 1 & h & 1 & & & & & & \\ & & & \cdots & & & & & & \\ & & & & 1 & h+1-k^* & k^* & & & \\ & & & & & k^* & h+1-k^* & 1 & & \\ & & & & & & & \cdots & & \\ & & & & & & & 1 & h & 1 \\ & & & & & & & & 1 & h \end{pmatrix} . \qquad (11)$$

In Equation (11), the diagonal entries $h + 1 - k^*$ occur in the row numbers $j - 1$ and j. Meanwhile the right-hand side vector b is given by $b = [-\gamma\ 0 \ldots 0]^{\mathrm{T}}$ and the unknown vector X consists of the responses $\tilde{x}_i$, $i = 1, 2, .., N$ of each mass to the excitation force in the Laplace domain.

The coefficient matrix A can further be manipulated and written in the form $A = A_h + P_j$ where $A_h = \begin{pmatrix} h & 1 & & & & \\ 1 & h & 1 & & & \\ 0 & 1 & h & 1 & & \\ & & \ddots & \ddots & \ddots & \\ & & & 1 & h & 1 \\ & & & & 1 & h \end{pmatrix}$ is the tridiagonal $N \times N$ matrix obtained by taking the Laplace transform of the homogeneous (nondefective) System (7) and P_j is the sparse $N \times N$ matrix

$$P_j = A - A_h = \begin{pmatrix} & & 0 & & & \\ & & \vdots & & & \\ 0 & \ldots & 1-k^* & k^*-1 & \ldots & 0 \\ 0 & \ldots & k^*-1 & 1-k^* & \ldots & 0 \\ & & \vdots & & & \\ & & 0 & & & \end{pmatrix}$$

whose only four nonzero entries occur at $j-1^{\text{st}}$ and j^{th} rows of the $j-1^{\text{st}}$ and j^{th} columns. The results from (Hu and O'Connell 1996) suggest that since the diagonal entries h of A_h involving the Laplace domain variable $s > 0$ and the damping coefficient $d > 0$ satisfy

$$h = -(s^2 + ds + 2) < -2$$

then A_h is invertible with inverse given explicitly by

$$R = A_h^{-1} = \left(R_{m,p}\right)$$

where following Hu's notations,

$$R_{m,p} = \frac{\cosh[(N+1-|p-m|)\lambda] - \cosh[(N+1-m-p)\lambda]}{2\sinh\lambda\sinh(N+1)\lambda}$$

and λ satisfies $h = -2\cosh\lambda$. Thus, System (10) can be expanded as

$$\begin{aligned} Ax &= b \\ \left(A_h + P_j\right)x &= b \\ R\left(A_h + P_j\right)x &= Rb \\ x + RP_jx &= Rb \end{aligned}$$

Note that since P_j is sparse, consisting only of four nonzero entries, the matrix product RP_jx can easily be computed. In fact, for any $i = 1, 2, \ldots, N$ we have

$$\tilde{x}_i + R_{i,j-1}\left((1-k^*)\tilde{x}_{j-1} + (k^*-1)\tilde{x}_j\right) + R_{i,j}\left((k^*-1)\tilde{x}_{j-1} + (1-k^*)\tilde{x}_j\right) = -R_{i,1}\gamma. \quad (12)$$

In particular, taking $i = 1$ in Equation (12) gives us the following expression for the Laplace domain response $\tilde{x}_1$ of the first mass to the impulse force in terms of $\tilde{x}_{j-1}$ and $\tilde{x}_j$

$$\tilde{x}_1(s) = -\gamma R_{1,1} - (1-k^*)(R_{1,j-1} - R_{1,j})\,\tilde{x}_{j-1}(s) - (1-k^*)(R_{1,j} - R_{1,j-1})\tilde{x}_j(s). \quad (13)$$

Meanwhile, separately using $i = j-1$ and $i = j$ in Equation (12) and algebraically manipulating the resulting equations give us the following system obeyed by the responses $\tilde{x}_{j-1}$ and $\tilde{x}_j$ of the masses immediately adjacent to the defective spring

$$\begin{cases} (1-k^*)\left(R_{j,j-1} - R_{j,j}\right)\tilde{x}_{j-1} + \left(1 + (R_{j,j} - R_{j,j-1})(1-k^*)\right)\tilde{x}_j & = -\gamma R_{j,1} \\ \left(1 + \left(R_{j-1,j-1} - R_{j-1,j}\right)(1-k^*)\right)\tilde{x}_{j-1} + \left(R_{j-1,j} - R_{j-1,j-1}\right)(1-k^*)\tilde{x}_j & = -\gamma R_{j-1,1} \end{cases}. \quad (14)$$

Solving the preceding system of linear equations in the unknowns $\tilde{x}_{j-1}$ and $\tilde{x}_j$ gives

$$\begin{cases} \tilde{x}_{j-1} & = -\dfrac{-\gamma R_{j,1}V + \gamma R_{j-1,1}G}{GU - FV} \\ \tilde{x}_j & = -\dfrac{\gamma R_{j,1}U - \gamma R_{j-1,1}F}{GU - FV} \end{cases}, \quad (15)$$

where $F = (1-k^*)\left(R_{j,j-1} - R_{j,j}\right)$,
$G = 1 + \left(R_{j,j} - R_{j,j-1}\right)(1-k^*)$,
$U = 1 + \left(R_{j-1,j-1} - R_{j-1,j}\right)(1-k^*)$ and
$V = \left(R_{j-1,j} - R_{j-1,j-1}\right)(1-k^*)$. Using the equations in System (15) into Equation (13) yields an explicit expression for the response of the first system as a function of the parameters j and k^* representing the defect location and defect size, respectively. Ideally, this analytic expression for $\tilde{x}_1$ will be compared to the data obtained by directly measuring the Laplace domain response of the first mass in a physical system with a defective spring. In this paper however, we instead compare $\tilde{x}_1$ to a synthetic data obtained by independently solving System (9). This process is discussed in the following subsection.

The Optimization Algorithm

The proposed method identifies the defective spring in the system whose first mass is excited by the impulse force δ. This is done by minimizing the discrepancy between the analytically computed response of the first mass and the noisy synthetic data that mimics measurements from a physical setting. Let $\tilde{x}_{1,\text{analytic}}$ be the analytically computed response, defined as $\tilde{x}_1$ in Equation (13) with System (15), of the first mass. Since we assume that our scheme has no access to the location and size of the defect, we consider $\tilde{x}_{1,\text{analytic}}$ as a function of the location j of the defect, the size k of the defect, and the Laplace variable s. Meanwhile, we let $\tilde{x}_{1,\text{synthetic}}$ denote the synthetic data that mimic perfect real-life measurements in the Laplace domain. To simulate measurement uncertainty, a Gaussian noise ϵ is added to the synthetic data. The measurement noise is quantified by its relative size with the synthetic data. The objective function to be minimized is

$$f(j,k) = \log\left(\int_0^{+\infty} \left[\tilde{x}_{1,\text{analytic}}(j,k,s) - \left(\tilde{x}_{1,\text{synthetic}}(s) + \epsilon(s)\right)\right]^2 ds\right),$$

which is the logarithm of the squared L^2- norm of the residual. The logarithm ensures that the optimizer (fmincon) avoids premature termination due to very small jumps in the objective function values between iterations. The introduction of the noise function ϵ makes this approach better reflect the conditions of practical defect detection, where the measurements are inevitably corrupted by noise.

In practice we run the local optimizer (MATLAB fmincon) independently for each candidate defect index $j \in \{2,\ldots,N\}$ and pick the (j,k) pair with minimal residual. This exhaustive per index procedure reduces the optimizer's sensitivity to local minima in the variable k and keeps the inversion computationally cheap (by just performing one forward solve per j). The optimizer employs gradient-based methods to search for a local minimum of a user-defined objective function, subject to linear and nonlinear constraints, as well as bound restrictions. Because it is a local solver, its success depends strongly on the smoothness of the objective landscape and the choice of initial guess. For each candidate j, fmincon is executed to estimate the optimal k that minimizes the residual. This process is repeated for all $j \in \{2,\ldots,N\}$, and the pair (j,k) that produces the minimum value of the objective function is selected as the location and estimated size of the defect.

RESULTS AND DISCUSSION

In this section, we present the defect characterization scheme that aims to find the location and size of the single defective spring in a system of arbitrary length. All computations are performed on a nondimensional 1D chain of length $L = 1$ with $N = 100$ cells and $\Delta x = \frac{1}{N}$. For convenience, we set the nondimensional cross-section $A = 1$ and the nominal mass and stiffness per cell to $m_i = 1, k = 1$. To map results to physical units, one can choose a physical cross-section A_{phys}, density ρ and baseline Young's modulus E_0. The physical cell length is $\Delta x_{phys} = \frac{L_{phys}}{N}$, and

$$m_i^{phys} = \rho A_{phys} \Delta x_{phys}, \qquad k_i^{phys} = \frac{E_i A_{phys}}{\Delta x_{phys}}.$$

Hence the conversion factors are $m_{ref} = \rho A_{phys} \Delta x_{phys}$ and $k_{ref} = \frac{E_0 A_{phys}}{\Delta x_{phys}}$, and physical time/frequency follow

$$t^{phys} = t\sqrt{\frac{m_{ref}}{k_{ref}}}, \quad \text{and } \omega^{phys} = \omega\sqrt{\frac{k_{ref}}{m_{ref}}},$$

where t, ω denote the time and frequency, respectively and $\sqrt{\frac{m_{ref}}{k_{ref}}} = \frac{\Delta x_{phys}}{c}$ with $c = \sqrt{\frac{E_0}{\rho}}$, so a nondimensional time unit equals the travel time across one cell.

We illustrate the effect of measurement noise to this approach necessitating the need for the introduction of what we call the σ-smooth approach. This modification in the objective function, coupled with a Monte Carlo run, mitigates the effect of the noise to the system. The section ends with an illustration of a more analytic approach that can be an alternative for scenarios when the defect is located near the end of the system.

A Noise-free Simulation

In this section, we demonstrate that the good performance of the proposed optimization procedure for noise- free data. Figure 3 shows the synthetic data generated with the following parameters: number of masses $N = 100$, damping coefficient $d = 0.1$, impulse intensity $\gamma = 1$, uniform spring constant $k = 1$, defect location $j_{\text{true}} = 40$, and defect spring constant $k^* = 1.3$. In other words, the system contains a single defective spring in position $j_{\text{true}} = 40$ with stiffness $k^* = 1.3$, while all other springs have $k = 1$.

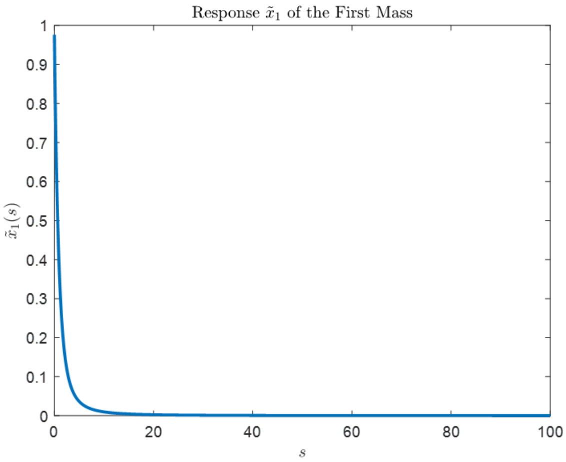

Figure 3: Graph of Synthetic Data for the system with parameters $\boldsymbol{N = 100, d = 0.1, \gamma = 1, j = 40}$, and $\boldsymbol{k^* = 1.3}$.

To identify the defect, the optimization routine fmincon was executed 99 times, once for each possible location of the defect $j \in \{2,\ldots,100\}$. For each j, the optimizer solved for the optimal defect size k that minimizes the objective function $f(j,k)$. Figure 4 shows the corresponding minimal residual values with respect to k, calculated as $10^{f(j,k)}$ for each possible value of j. Here, the x −axis corresponds to the possible defect locations j, while the y −axis represents the residual magnitude $10^{f(j,k_j^*)}$, where k_j^* is the minimizer of the objective function for each fixed value of j.

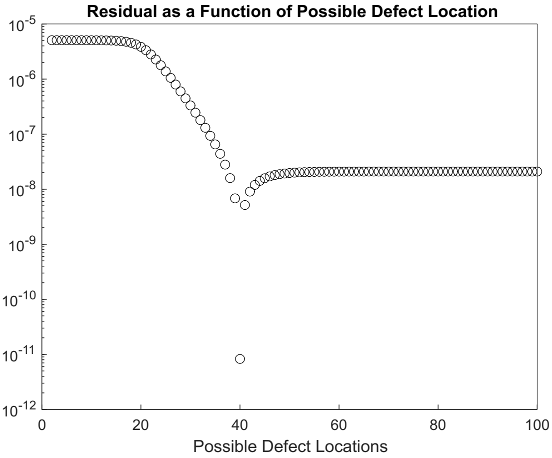

Figure 4: Residual as a function of the possible defect location.

The results indicate that the smallest residual occurs at $j = 40$, matching the true defect location. The corresponding computed defect stiffness is $k^* \approx 1.299848$, which is in excellent agreement with the true value $k^* = 1.3$. The relative error is $\frac{|k^*_{\text{comp}}-k^*|}{k^*} \approx 1.17 \times 10^{-4}$, demonstrating high accuracy. This suggests that given a perfect set of measurement values of the system response, the proposed method yields highly reliable results. The next subsection shows the effect of the introduction of various noise levels to the measurements.

Effect of Gaussian Noise

Modern laboratory Laser Doppler Vibrometers (LDV) achieve sub-nanometer to picometer- class displacement noise floors depending on bandwidth and surface reflectivity; assuming a conservative axial displacement noise of order 10^{-6} m for our experimental bandwidth is realistic (see Ofv-5000 2025, Rothberg et al 2017). Thus, we test our algorithm for sensitivity to noise of magnitude within the threshold of modern LDVs.

Figure 5 and Figure 6 show the effect of the Gaussian noise ϵ on the accuracy of defect detection. We again consider the defective system with the same parameters as the ones used in Section 3.1.

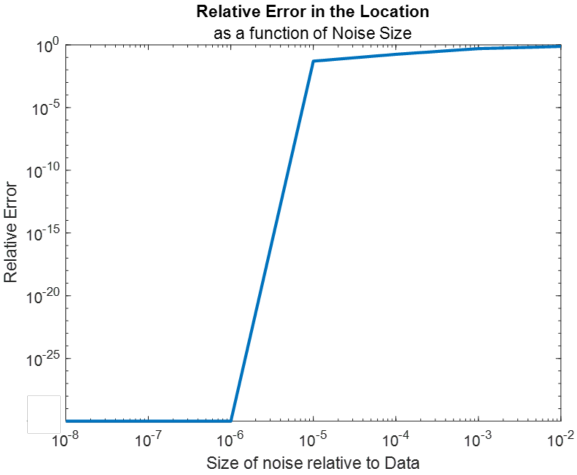

Figure 5: Relative error in the estimate for the defect location as a function of noise level for the system with parameters $\boldsymbol{N = 100, d = 0.1, \gamma = 1, j = 40}$, and $\boldsymbol{k^* = 1.3}$.

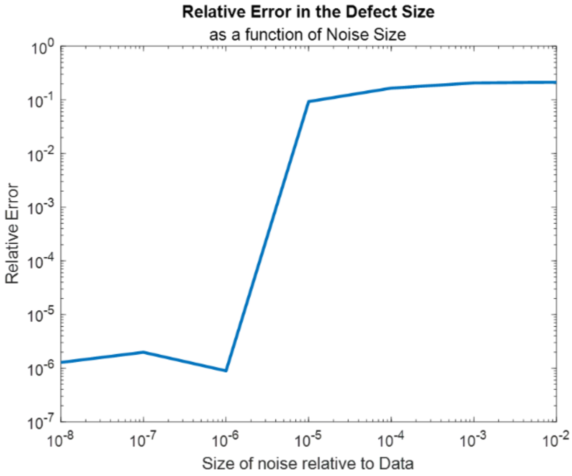

Figure 6: Relative error in the estimate for the defect size as a function of noise level for the system with parameters $\boldsymbol{N = 100, d = 0.1, \gamma = 1, j = 40}$, and $\boldsymbol{k^* = 1.3}$.

Figure 5 plots the relative error in the predicted defect location as a function of the relative size of ϵ. For ϵ of magnitude $10^{-8}, 10^{-7}$, and 10^{-6} relative to the synthetic data, the predicted defect location matches the true location exactly. However, when the noise level is at 10^{-5}, the relative error in the predicted location increases to approximately 5%, and it continues to grow as the noise level increases. This suggests a noise level threshold near of 10^{-6} beyond which location detection degrades significantly. Meanwhile, Figure 6 shows the relative error in computed defect size as a function of noise level. At noise level 10^{-5}, the relative error in the estimated defect size is about 9.30%, whereas for $\epsilon = 10^{-6}$, the error is on the order of 10^{-6}. This confirms that 10^{-6} serves as a practical noise level threshold for accurate detection. Notably, this noise level is still well within the capabilities of modern defect detection systems, which can achieve precision up to 10^{-12}.

In the next subsection, we present a modification of the basic optimization algorithm that mitigates the effect of the measurement noise. We shall see that this approach improves the noise level threshold by some orders.

The σ −smooth Approach

To further improve robustness against noise, we propose a variant of the optimization procedure, which we refer to as the σ-smooth approach. The framework remains the same: we begin with the synthetic data $\tilde{x}_{1,\text{synthetic}}$, add Gaussian noise ϵ of prescribed size, and then minimize the residual between the analytic and measured responses. The key modification is the introduction of a random perturbation to the defect size parameter k in the objective function.

In the original formulation, the optimizer solves directly for k. In the σ-smooth approach, however, the unknown k is replaced by

$$k + \delta$$

where δ is a random perturbation drawn from a normal distribution with mean zero and variance σ^2, i.e., $\delta \sim N(0, \sigma^2)$. Thus, instead of estimating a single deterministic value of k, the method effectively searches for an interval $[k - \Delta, k + \Delta]$ of admissible values. This allows the solution to remain stable under noisy conditions, since small shifts in k within this interval still produce consistent results.

To account for randomness in δ, we generate N_δ independent samples $\{\delta_i\}_{i=1}^{N_\delta}$ from the distribution above. For each δ_i, we evaluate the modified objective function

$$f(j,k;\delta_i) = \log\left(\left(\int_0^{+\infty}\left[\tilde{x}_{1,\text{analytic}}(j,k+\delta_i,s) - \left(\tilde{x}_{1,\text{synthetic}}(s) + \epsilon(s)\right)\right]^2\right)^{\frac{1}{2}}\right).$$

The σ-smooth objective is then defined as the average:

$$F(j,k) = \frac{1}{N_\delta}\sum_{i=1}^{N_\delta} f(j,k;\delta_i).$$

Minimization is performed on F with respect to k, while j is treated as a discrete variable as before. When $\sigma = 0$, the method reduces to the deterministic formulation. For $\sigma > 0$, the perturbation introduces robustness by mitigating the effect of Gaussian noise in the measured data. In practice, we found that setting $\sigma = 10^{-4}$ and averaging over $N_\delta \approx 50$ samples is sufficient to stabilize the results.

Note that Monte Carlo runs were also employed in the σ-smooth approach to account for the presence of noise and the stochastic nature of the defect detection problem. By repeating the optimization procedure over multiple randomized noise realizations, we were able to obtain statistically reliable estimates of the residual functional and the optimizer's performance. This averaging process reduces sensitivity to a single noise instance and highlights the overall trend of defect detectability across different locations. The final estimates for the defect location and defect size are taken to be the median of the respective estimates from each Monte Carlo run.

A Simulation Employing the σ-smooth Approach

To assess the performance of the σ-smooth approach, we compared its results against the deterministic method under noisy conditions. In particular, we tested the method by considering the defective system with the same parameters as in Section 3.2 but with noise of size 5×10^{-5}. The results are shown in Figure 7.

Without regularization (i.e., using the deterministic approach), the relative error in defect location was approximately 2.5%, while the relative error in the computed defect size was about 5.75%. These results indicate noticeable degradation in accuracy under noise.

In contrast, when the σ-smooth approach with $N_\delta = 50$ was applied to 100 Monte Carlo runs with each run having a different noise function, the performance improved significantly. The resulting estimates for the defect location and defect size for the simulation described above are plotted in Figure 7 and Figure 8, repsectively. Recall that the final estimates for the defect location and defect size were taken to be the median of the respective estimates from all the Monte Carlo runs. The median was chosen as multiple runs suggest that the optimization have the tendency to produce outlier estimates. The median provides a more robust measure of central tendency in the presence of these outliers or even skewed distributions of the results. The presence of outliers in the current simulation can be observed in Figure 7 and Figure 8. The relative error in defect location decreased from 2.5% to 0%, meaning the defect was identified exactly. Similarly, the relative error in the computed defect size dropped from 5.75% to 1.8×10^{-4}, demonstrating several orders of magnitude improvement. These results suggest that the proposed σ-smooth approach is effective in mitigating the influence of noise. Figure 7 illustrates the defect location identified in each simulation run, while Figure 8 shows the corresponding results for the defect size. In both figures, we can observe that a significant portion of the Monte Carlo runs produced estimates that are substantially different from the true defect location and true defect size. This shows that indeed, measurement noise significantly affects the defect characterization scheme as the skew some of the optimization results. However, the use of the median across all Monte Carlo runs mitigated the effect of the outliers and skewed results.

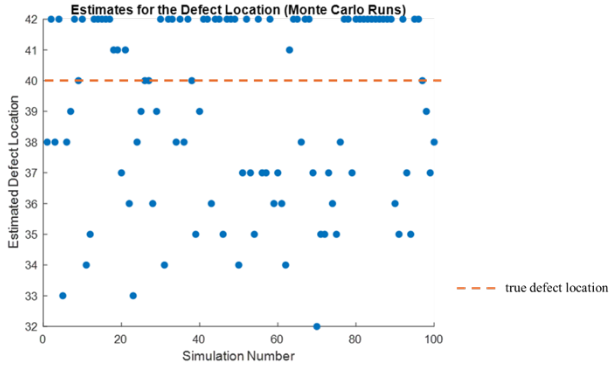

Figure 7: Estimates for the defect location from 100 Monte Carlo runs of the σ-smooth Approach.

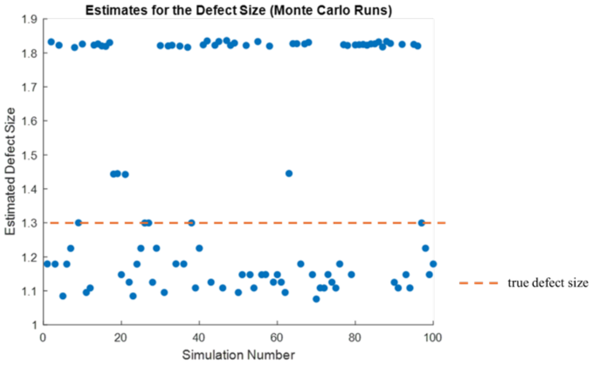

Figure 8: Estimates for the defect size from 100 Monte Carlo Runs σ-smooth Approach.

Multiple Simulation Runs

In this subsection, we investigate the limits of the robustness of σ-smooth approach. We reuse the σ-smooth approach with $N_\delta = 50$ draws across 100 Monte Carlo runs for defective systems with varying defect location and defect sizes. The common parameters among these systems are the uniform spring constant $k = 1$, damping coefficient $d = 0.1$, and number of masses $N = 100$. In all the experiments, the noise level was set to 5×10^{-4}.

Defect Detection for Fixed Defect Size and Varying Location

First, we employ the σ-smooth approach to characterize the defect in systems with a defective spring of stiffness $k^* = 1.30$ but varying locations j across the chain. Figure 9 shows the estimated defect size as a function of the true defect location. For most defect locations, the optimizer is able to recover the defect size accurately, yielding values close to $k^* = 1.30$. Meanwhile, Figure 10 shows the relative error in the defect size estimates as a function of the true defect location. One can observe from Figure 10 that beginning around $j = 79$, the optimizer experiences increasing difficulty in estimating the defect size, resulting in unstable or significantly overestimated values.We observe that up to $j = 78$, the relative error remains below the 5% threshold. Beyond this point, however, the relative error grows rapidly, indicating a degradation in the scheme's accuracy when the defect is located near the end of the system.

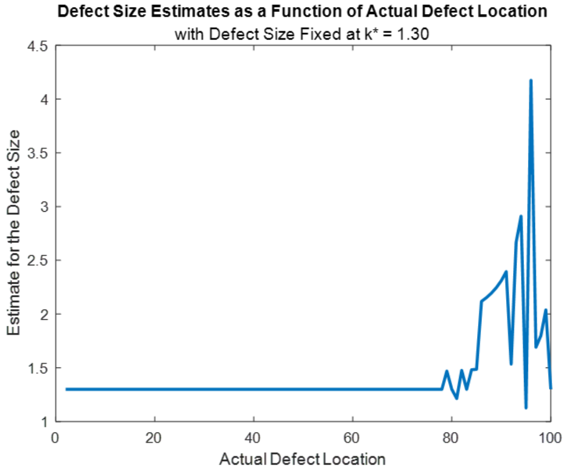

Figure 9: Estimate for the Defect Size vs Actual Defect Location for the Simulation in Section 3.5.1.

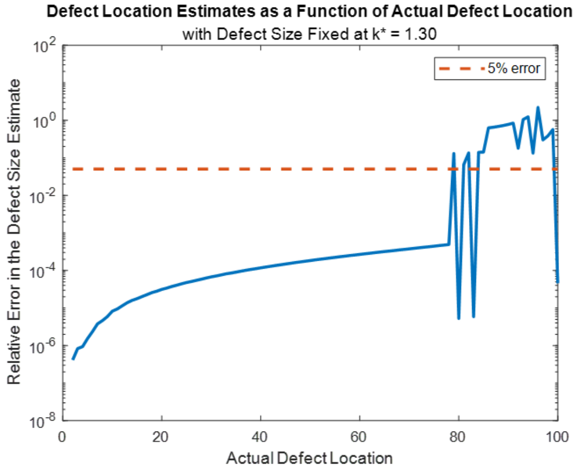

Figure 10: Relative Error in the Defect Size Estimate vs Actual Defect Location for the Simulation in Section 3.5.1.

Figure 11 shows the estimated defect location versus the true defect location. The optimizer performs very well in this task, producing estimates that closely follow the diagonal line (perfect agreement). The corresponding relative error, shown in Figure 12, confirms this: the location is always predicted within at most 2.33% error, which corresponds to a maximum of two positions away from the true defect location.

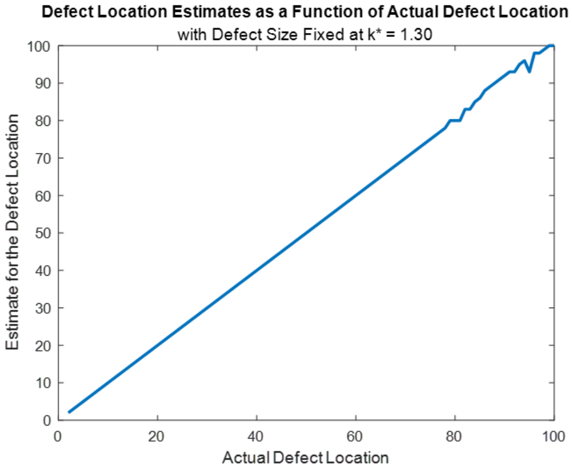

Figure 11: Estimate for the Defect Location vs Actual Defect Location for the Simulation in Section 3.5.1.

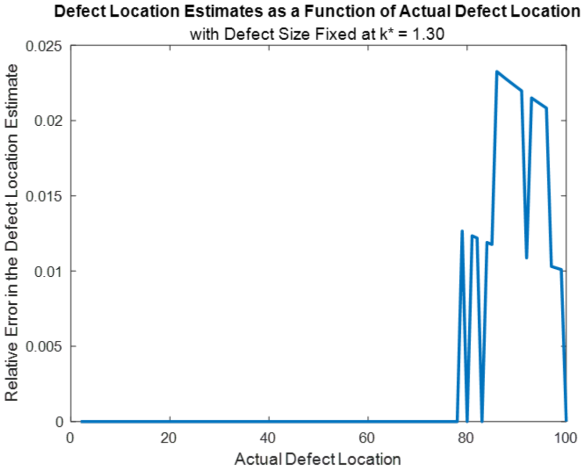

Figure 12: Relative Error in the Defect Location Estimate vs Actual Defect Location for the Simulation in Section 3.5.1.

In summary, for a fixed defect size $k^* = 1.30$, the optimizer reliably identifies the defect location across the entire domain, but struggles to estimate the defect size accurately once the defect is positioned near the end of the system. This makes sense from the physical point of view as the exciting force dissipates fast as it travels across the chain. Hence, the effect of the defect to the vibrations in the first mass becomes less and less as the defect's location becomes close to the other end. One way to handle such cases is to incorporate measurements from the last mass in the optimization. This will be explored in upcoming studies.

Defect Detection for Fixed Location and Varying Defect Size

Now, we fix the defect location at $j = 40$ and vary the defect size k^*. Figure 13 shows the estimated defect size as a function of the true defect size. The estimates align almost perfectly with the diagonal, indicating that the scheme is highly successful in recovering the true defect size across the tested range. Figure 14 which shows the corresponding relative error in the defect size estimate, further confirms this observation. It shows that the maximum error is just around 2.77%.

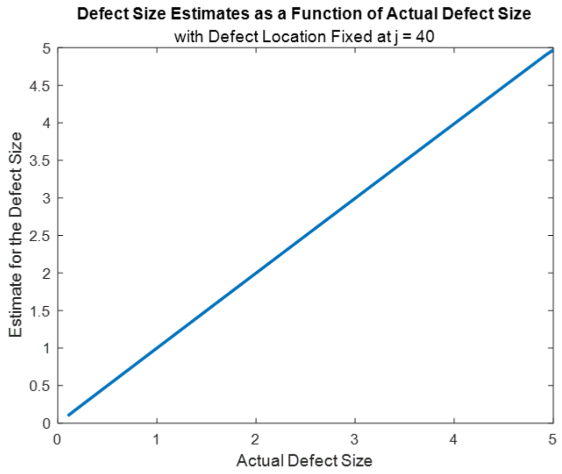

Figure 13: Estimate for the Defect Size vs Actual Defect Location for the Simulation in Section 3.5.2.

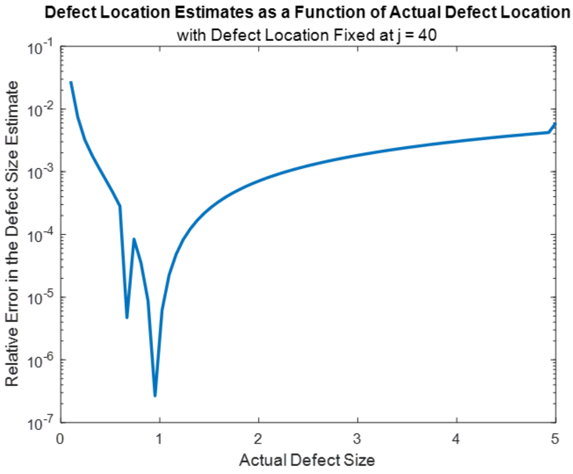

Figure 14: Relative Error in the Defect Size Estimate vs Actual Defect Location for the Simulation in Section 3.5.2.

Figure 15 shows the estimated defect location as a function of the true defect size. Here, the estimates remain constant at the true defect location $j = 40$. Figure 16 displays the relative error in the defect location estimate as a function of actual defect size. From there, one can observe that the defect locations are always exactly calculated.

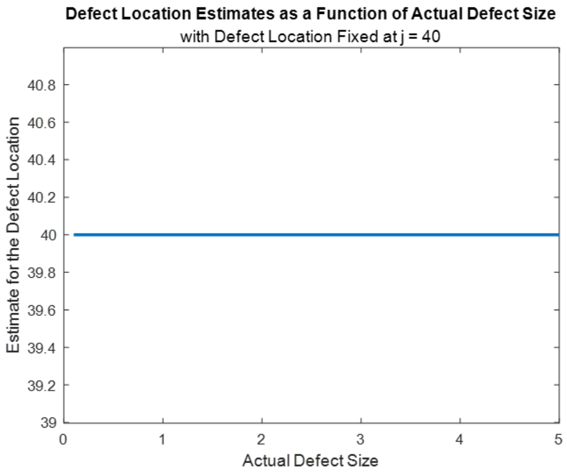

Figure 15: Estimate for the Defect Location vs Actual Defect Location for the Simulation in Section 3.5.2.

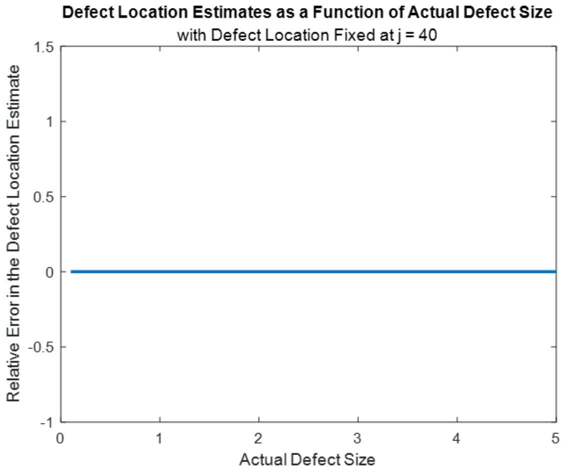

Figure 16: Relative Error in the Defect Location Estimate vs Actual Defect Location for the Simulation in Section 3.5.2.

These multi-case simulations show that the defect characterization scheme utilizing several Monte Carlo runs of the σ-smooth approach works well with most systems of various defect locations and defect sizes even when the measurement data are tainted with noise of size 5×10^{-4}. The exemptions are the cases when the defect is located near the end of the system. To address these cases, we mentioned a possible extension of the current approach which incorporates the measurements from the other end of the system. Another approach, albeit more mathematically involved and computationally expensive is to simply plot the residual as symbolic functions of j and k. This approach is illustrated in the next subsection.

An Analytic Approach: Sketching the Graph of the Residual Function

To address the cases when the defect is located near the end of the system, we employ a purely analytic approach. This time, we treated all quantities as symbolic functions and directly evaluated the residual

$$f(j,k) = \log\left(\int_0^{+\infty} \left[\tilde{x}_{1,\text{analytic}}(j,k,s) - \left(\tilde{x}_{1,\text{synthetic}}(s) + \epsilon(s)\right)\right]^2 ds\right),$$

as a function of the possible defect locations j and defect sizes k. For these experiments, we introduced a noise of magnitude 5×10^{-4}. By evaluating $f(j,k)$ across a range of defect locations and defect magnitudes and plotting the results as a three-dimensional surface, we can visually identify the location and size of the defect.

First, we consider the case of a system with the following parameters: $N = 100, d = 0.1, k = 1$, $k^* = 1.3, j^* = 85$. The residual $10^{f(j,k)}$ is plotted in Figure 17. Here, we see spikes in the surface, indicating the extreme values of the residuals. Two dimensional slices of this surface are shown in Figure 18 and Figure 19, indicating that the global minima indeed occur at $j = 85$ and $k = 1.3$.

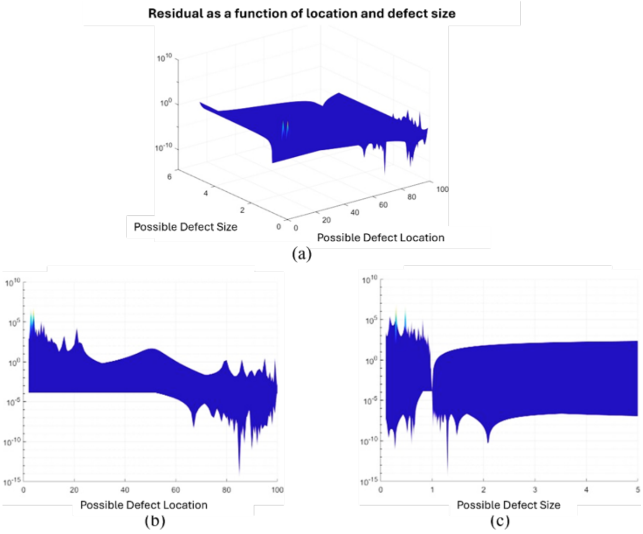

(a)

(b) (c)

Figure 17: Graphs of the residual as a function of location and defect size in the system with $\boldsymbol{N} = \mathbf{100}, \boldsymbol{d} = \mathbf{0.1}, \boldsymbol{k} = \mathbf{1}, \boldsymbol{k}^* = \mathbf{1.3}, \boldsymbol{j} = \mathbf{85}$: (a) Full 3D graph, (b) 2D slice showing the residual as a function of possible defect location, and (c) 2D slice showing the residual as a function of possible defect size

These plots also indicate why the optimization routine employing fmincon is having some difficulties in characterizing the defect. The frequent oscillations of the residual function create multiple local minima. The MATLAB fmincon, being a local solver might had been trapped in one of these local minima and hence, converged to an inaccurate estimate for the defect location and/ or defect size.

The next simulation shows a very similar scenario, with $N = 100, d = 0.1, k = 1, k^* = 1.1$, and $j^* = 90$. Here we have a smaller defect located further in the system. Again, we see in Figure 18 the 3D rendering of the residual as a function of the possible defect locations and defect sizes. Multiple spikes are again observed, showing the peaks and valleys of the residual.

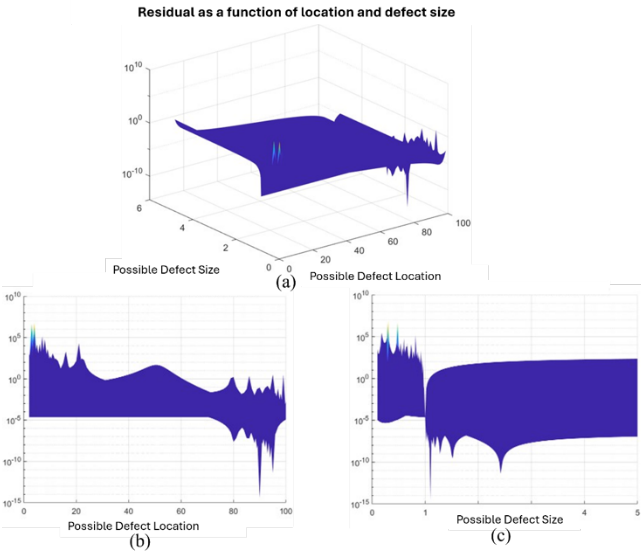

(a)

(b) (c)

Figure 18: Graph of the residual as a function of location and defect size for the system with $\boldsymbol{N} = \mathbf{100}, \boldsymbol{d} = \mathbf{0.1}, \boldsymbol{k} = \mathbf{1}, \boldsymbol{k}^* = \mathbf{1.1}$, and $\boldsymbol{j}^* = \mathbf{90}$: : (a) Full 3D graph, (b) 2D slice showing the residual as a function of possible defect location, and (c) 2D slice showing the residual as a function of possible defect size

These cases show an alternative way of characterizing the defect. This is extremely useful especially for cases when the defect is located further down the system. However, this approach is mathematically tedious and computationally expensive as all variables are treated to be symbolic.

CONCLUSION

In this paper we studied the problem of imaging the location and size of a single defect in the Young's modulus for a long metal bar of length L and cross-sectional area $A = 1$. The model was idealized as a 1D bar and was shown equivalent to a discrete spring-mass system.

We proposed a robust algorithm for characterizing one defect in a spring-mass system under the action of an impulsive force. In our particular numerical example, the setup we used was with a bar of length $L = 1$ discretized to $N = 100$ finite difference points. This will resolve only modes up to the model dependent cut-off frequency. In fact, with spatial spacing $h = \Delta x$ and wave speed $c = \sqrt{\frac{E_0}{\rho}}$, the model reliably resolves frequencies up to

$$f_{max} \approx \frac{c}{4h} = \frac{cN}{4L}.$$

(In practice one must choose N so that fmax exceeds the highest physical frequency of interest; the factor 4 is a conservative margin to limit numerical dispersion.)

This type of forcing is a good approximation of a regular band limited forcing since the high order modes are carrying very little energy and contribute insignificantly to the measurement map and thus can be neglected. In fact, in our numerical setup for the $L = 1$, and $N = 100$ we can resolve approximately 50 modes. The unresolved modes have amplitude less than $O(1/N) \times \delta$, i.e., 1% of the main vibrational amplitude. We also tested our systems for robustness against Gaussian noise of size $\epsilon \in (10^{-8}, 10^{-2})$. In practice, one should assume a noise level $\epsilon \approx 10^{-2} \cdot \delta$ where δ denotes the typical displacement amplitude in the system considered (e.g., for example in our numerical setup of $L = 1$ bar with $N = 100$ masses, $\delta \approx 10^{-4}$). For this level of noise, we showed that our method remains robust.

The proposed approach minimizes the discrepancy between the analytically computed response map, i.e., vibrations of the first mass as a function of the defect location and size and the synthetic data map that mimics measurements in a physical setting, i.e., the vibrations of the first mass when the system with one defect is activated by the impulsive force at the first mass. The approach entails a minimization procedure that seems to be sensitive to measurement noise. To mitigate the effect of noise, a smoothing technique, referred to here as the σ-smooth approach is employed to modify the objective functional. This, coupled with multiple Monte Carlo runs proved to make this approach a couple of orders less sensitive to measurement noise.

The proposed scheme works well against Gaussian noise and characterizes well the defect size and location for defects located not too close near the right end of the bar. The proposed optimization strategy appears to have some difficulties in characterizing defects that occur near the other end point of the system. This may be due to two factors, namely the quick dissipation of the energy in the system due to the assumed damping and the highly oscillating behavior of the residual functional. We proposed an analytic approach for such cases. Numerical results indicate that this approach works in detecting the exact size and location of defects located near the right end of the bar but it tends to be computationally expensive. An alternative approach, one that incorporates in the objective functional measurements from the last mass in the system seems much more elegant and it will be considered in forthcoming studies.

ACKNOWLEDGMENTS

The authors received no external funding for this work.

CONFLICT OF INTEREST

The authors declare that there is no conflict of interest.

CONTRIBUTIONS OF INDIVIDUAL AUTHORS

Senior authors NJA Egarguin and DO Onofrei laid down the foundation of the study, including the statement of the problem and study objectives, designed the theoretical framework and provided a generic framework for the numerical simulations. Junior authors BNM Ong and A Borker provided the details for the numerical framework, and designed and implemented the numerical simulations. All authors contributed to writing the final manuscript.

REFERENCES

Ofv-5000 modular vibrometer, product brochure. https://www.polytecstore.fr/polytec_images/documents/oms/pb_ofv-5000.pdf. Accessed: 2025-09-01.

Cawley P, Adams R. The location of defects in structures from measurements of natural frequencies. Journal of Strain Analysis for Engineering Design 1979; 14: 49-57.

Dilena M, Morassi A. Structural health monitoring of rods based on natural frequency and antiresonant frequency measurements. Structural Health Monitoring 2009; 8(2): 149-173.

Dimarogonas AD. Vibration of cracked structures: A state-of-the-art review. Engineering Fracture Mechanics 1996; 55(5): 831-857.

Egarguin NJA, Guan L, and Onofrei D. Defect characterization in a 1D spring-mass system using the Laplace and z −transforms. Journal of Vibration Engineering & Technologies 2022; 10:1121-1134.

Egarguin NJA, Meklachi T, Onofrei D, Harari-Arnold N. Vibration suppression and defect detection schemes in 1D linear spring-mass systems. Journal of Vibration Engineering & Technologies 2020; 8: 489-503.

Grebla H, Rusu V, Gillich GR, Bui T. Assessment of cracks in beams using changes in the measured frequencies and particle swarm optimization. Vibroengineering Procedia 2023; 51: 29-34.

Hu GY, O'Connell RF. Analytical inversion of symmetric tridiagonal matrices. Journal of Physics A: Mathematical and General 1996; 29(7):1511.

Krawczuk M, Grabowska J, Palacz M. Longitudinal wave propagation. Part II—analysis of crack influence. Journal of Sound and Vibration 2006; 295(3): 479-490.

Liu F, Liu A, Wang L, Wei Y. Accurate modeling and wave propagation analysis of cracked slender structural members by the spectral element method. Structural Control and Health Monitoring 2023; 1:5569434.

Palacz M, Krawczuk M. Analysis of longitudinal wave propagation in a cracked rod by the spectral element method. Computers & Structures 2002; 80(24):1809-1816.

Peng K, Zhang Y, Xu X, Han J, Luo Y. Crack detection of threaded steel rods based on ultrasonic guided waves. Sensors 2022; 22(18).

Rothberg SJ, Allen MS, Castellini P, Di Maio D, Dirckx JJJ, Ewins DJ, Halkon BJ, Muyshondt P, Paone N, Ryan T, Steger H, Tomasini EP, Vanlanduit SJA, Vignola JF. An international review of laser doppler vibrometry: Making light work of vibration measurement. Optics and Lasers in Engineering 2017; 99:11-22, 2017.

Rubio L, Fernández-Sáez J, Morassi A. Identification of two cracks in a rod by minimal resonant and antiresonant frequency data. Mechanical Systems and Signal Processing 2015; 60-61:1-13.

Shifrin EI. Inverse spectral problem for a non-uniform rod with multiple cracks. Mechanical Systems and Signal Processing 2017; 96:348-365, 2017.

Zeng Z, Gao M, Ng CT, Sheikh AH. Guided wave-based characterisation of cracks in pipes utilizing approximate Bayesian computation. Thin-Walled Structures 2023; 192:111138.

Zhang S, Shen W, Li D, Zhang X, Chen B. Nondestructive ultrasonic testing in rod structure with a novel numerical Laplace based wavelet finite element method. Latin American Journal of Solids and Structures 2018; 15.

Zou Y, Tong L, Steven G. Vibration-based model-dependent damage (delamination) identification and health monitoring for composite structures - a review. Journal of Sound and Vibration 2000; 230: 357-378.